Roselló-Márquez, G.; Fernández Domene, RM.; Sánchez Tovar, R.; Garcia-Anton, J. (2020). Influence of annealing conditions on the photoelectrocatalytic performance of WO3 nanostructures. Separation and Purification Technology. 238:1-7. https://doi.org/10.1016/j.seppur.2019.116417

INFLUENCE OF ANNEALING CONDITIONS ON THE PHOTOELECTROCATALYTIC PERFORMANCE OF WO_3 NANOSTRUCTURES

Roselló-Márquez, G.[a]; Fernández-Domene, R.M. [a]; Sánchez-Tovar, R. [a,b]; García-Antón, J.[a]

[a] *Ingeniería Electroquímica y Corrosión (IEC), Instituto Universitario de Seguridad Industrial, Radiofísica y Medioambiental (ISIRYM), Universitat Politècnica de València, Camino de Vera s/n, 46022 Valencia, Spain.* [*] *jgarciaa@iqn.upv.es*

[b]*Departmento de Ingeniería Química, Universitat de València, Av de les Universitats, s/n, 46100 Burjassot, Spain*

ABSTRACT

Nanostructured WO_3 photoanodes have been synthesized by electrochemical anodization under controlled hydrodynamic conditions in acidic media in the presence of 0.05M H_2O_2. Subsequently, samples have been subjected to a thermal treatment (annealing) at different temperatures (400º C, 500º C and 600º C) and under different gaseous atmospheres (air, N_2, Ar). The influence of these annealing conditions on the morphology, crystallinity, photoelectrochemical behavior and dopant chemistry of the different photoanodes has been investigated through Electronic Microscopy, Raman Spectroscopy, Photoelectrochemical Impedance Spectroscopy and Mott-Schottky analysis. In general, higher annealing temperatures resulted in samples with higher degrees of crystallinity, which in turn favored the transport of electron-hole pairs through the semiconducting photoanodes. Besides, an increase in annealing temperature implied higher densities of donor species within the samples structure, which can explain the observed enhancement in charge transfer. Annealing temperature was observed to have a more marked impact on the photoelectrocatalytic performance of WO_3 nanostructures than the gaseous atmosphere.

Keywords: WO_3 nanostructures, photoanode, anodization, annealing conditions, photoelectrochemical impedance spectroscopy (PEIS).

1. INTRODUCTION

Tungsten oxide (WO_3) is considered as one of the most important photocatalytic materials due to its excellent properties such as its earth-abundance, its highly modifiable composition, high chemical stability in a range of moderate pH and excellent electrical conductivity [1–3], and its great variety of applications such as its use as a producer of clean energy. The global energy consumption is expected to increase even more during the next years as a result of the technological advances of society on a day-to-day basis. Nowadays, most of the consumed energy comes from fossil fuels [4] such as oil, coke and natural gas but they will end up being depleted in the future. Moreover, these fossil fuels are not sustainable, leading to the drastic climate change that is occurring through global warming, as well as generating other types of pollution. Then, there is a great need to find renewable and environmentally friendly energy sources to reduce the environmental impact of fossil fuels and the full cost that this impact entails.

WO_3 is composed of units of perovskite, making it one of the most attractive candidates for its use in photoelectrocatalysis (PEC), since it can absorb up to 12% of the solar spectrum with a band gap (E_g) between 2.5 and 2.8 eV, a moderate hole diffusion length (~ 150 nm) compared to α-Fe_2O_3 (2-4 nm) and better electron transport (ca.12 $cm^2\ V^{-1}\ s^{-1}$) compared to TiO_2 (0.3 $cm^2\ V^{-1}\ s^{-1}$) [5–8]. In addition, WO_3 is a n- type material, so it is used as a photoanode. It presents a high stability at low pH where the evolution of H_2 happens more efficiently. As mentioned above, WO_3 absorbs a greater part of the sunlight than TiO_2 and shows higher photocurrent densities in a steady state since it has a higher incident photon to current efficiency (IPCE) than the Fe_2O_3. Therefore, WO_3 is considered more appropriate than, for instance, TiO_2 and Fe_2O_3 for PEC applications. However, this material exhibits high recombination of the photogenerated electron-

holes during the PEC process, which is an inconvenient when PEC is carried out in practice [9].

The crystal structure of WO_3 is based on an ABO_3 perovskite structure with three-dimensional networks where WO_6 octahedra are shared in the corners. However, due to the distortions related to antiferroelectric displacements of the W atoms and the mutual rotation of the oxygen octahedra, the structure of WO_3 shows significant differences from the ideal perovskite structure showing five stable phases in a range of temperature that goes from 900ºC to -180ºC called tetragonal (α-WO_3), orthorhombic (β-WO_3), monoclinic I (γ-WO_3), triclinic (δ-WO_3) and monoclinic II (ε-WO_3) [10]. Due to the distortion of the original octahedra, WO_3 band gap increases significantly. This means that the crystallographic arrangement determines the band gap of the semiconductor, increasing from 1.6 eV to 2.4 eV of the monoclinic structure [11]. Among all crystalline structures, the monoclinic structure is the most stable and the most efficient in PEC applications [12,13]. In addition to the crystal structure, the crystalline facet also has a great effect on the PEC processes where WO_3 participates since the overpotential that is required for photooxidation on the surface of WO_3 is totally conditioned on the orientation of the crystals [14]. Among all the crystalline facets, (002) is the most suitable for adsorption, redox reactions and degradations of organic pollutants [15]. It has been shown that the facet (002) of WO_3 facilitates the separation of photo-induced charges carrier and represses the formation of peroxo-species, producing a higher photocurrents and better photostability.

It has been reported that 2D nanostructures (nanoflake / nanoplate / nanosheet) have improved properties with respect to 1D nanostructures since they can orthogonalize the directions of the absorption of the incident light by the long axes and charge carriers can move through the short radius, causing greater efficiency in the absorption of light and

in the collection of charge carriers, resulting in higher PEC efficiencies. In addition, the characteristic porous morphology allows photogenerated minority carriers to be accumulated in an orthogonal direction over short distances. With low minority carrier accumulation distances, high quantum yields (both external and internal) can be produced for accumulation of photogenerated charges [10].

Another important parameter to study is the temperature of the heat treatment that is given to the samples after their synthesis (annealing), since it has a great effect on the nanostructures converting their amorphous structure to a crystalline one. As the layers of WO_3 contain a hydrated region, and therefore an amorphous structure, it must be transformed into a crystalline one to be used as electrochromic devices, in photoelectrochemical and photocatalytic processes, etc [16,17]. Heat treatment at high temperatures has been demonstrated to achieve that change, having a great influence on the morphology of the surface, on the crystal structure and on the phase transition [18,19].

In a previous work [20], it was observed that high annealing temperatures (600º C) enhanced the PEC performance of WO_3 nanosheets/nanorods, increasing their efficiency as photoanodes for the degradation of persistent organic pollutants, such as the pesticide chlorfenvinphos. However, an exhaustive investigation about the influence of annealing conditions (temperature and atmosphere) on the PEC properties of WO_3 nanostructures is required. It is therefore necessary to develop and implement extensive characterization procedures, especially from an electrochemical and photoelectrochemical point of view, to systematically study the influence of different parameters on the photoelectrochemical performance of new nanostructured photoanodes. This is the main objective and the novelty of the present work. To accomplish this objective, the structural, morphological and photoelectrochemical

properties of WO_3 nanostructures formed at various temperatures (400º C, 500º C and 600º C) and under different atmosphere (air, N_2 and Ar) were evaluated through Field Emission Scanning Electronic Microscopy (FESEM), Confocal Raman Spectroscopy, Photoelectrochemical Impedance Spectroscopy (PEIS) and Mott-Schottky analysis.

2. EXPERIMENTAL PROCEDURE

2.1. Nanostructures fabrication

WO_3 nanostructures were fabricated by electrochemical anodization of tungsten cylinders (8 mm in diameter). Tungsten substrates were wet abraded with polishing paper grade 220, 1000 and 4000, rinsed with distilled water and dried with compressed air. Anodization was carried out in a 1.5 M H_2SO_4 + 0.05 M H_2O_2 solution, using a platinum mesh as the cathode of the electrochemical cell and the tungsten samples as the anode. Electrolyte temperature was 50º C and the cell potential 20 V. The tungsten electrode was continuously rotated at 375 rpm by using a Rotating Disk Electrode (RDE). The circular area of the electrode exposed to the electrolyte was 0.5 cm^{-2}. After 4 h of anodization, samples were annealed in a tubular oven using different temperatures (400º C, 500º C and 600º C; higher temperatures were also used but nanostructures were collapsed) and different gaseous atmospheres (air, N_2 and Ar).

2.2. Morphological and structural characterization

Field Emission Scanning Electronic Microscopy (FESEM) images were taken using a Zeiss Ultra 55 microscope, at 2 kV. Raman spectra were obtained with a confocal Raman microscope with a blue neon laser (488 nm).

2.3. Photoelectrochemical characterization

Photoelectrochemical characterization of the WO_3 nanostructures was performed using a transparent quartz cell of 14 mL with a three-electrode configuration: a platinum tip counter electrode, an Ag/AgCl (3 M KCl) reference electrode and the nanostructures as the working electrodes. All tests were carried out in a 0.1 M H_2SO_4 electrolyte by using an Autolab PGSTAT302N potentiostat and under simulated sunlight (AM1.5 conditions) with a power intensity of 100 mW cm^{-2}.

WO_3 nanostructures were immersed in the photoelectrochemical cell without illumination and an external bias of 1 V was applied. After stabilizing dark current densities, samples were irradiated. Photocurrent densities were recorded for 30 minutes under these conditions. After that, Photoelectrochemical Impedance Spectroscopy tests (PEIS) were carried out from 10 kHz to 10 mHz and applying a potential perturbation of 10 mV. Subsequently, Mott-Schottky plots were constructed at 5 kHz by scanning the potential from 1 V to 0.2 V at a rate of 50 mV s^{-1}.

3. RESULTS AND DISCUSSION

Figure 1 shows all the FESEM images for the different WO_3 samples after annealing in different atmospheres (air, N_2 and Ar) at different temperatures (400º C, 500º C and 600º C). Very small nanosheets or nanorods were formed in all the cases. Nevertheless, it can be observed that the morphology of these nanostructures became much more defined as annealing temperature increased. In fact, at 400º C and regardless of the annealing atmosphere, a nanosheet morphology with very small sizes was obtained, which was progressively transformed into nanorods at higher temperatures. At 600º C and for samples annealed in air and N_2 atmospheres (**Figure 1c** and **Figure 1f**, respectively), a clear nanorod array morphology can be observed. According to Fan et al. [21], this kind of nanostructure offers efficient electron transfer from the WO_3 to the back contact. The transformation from poorly defined nanosheets to clearly defined nanorods with increasing annealing temperature can be related to a higher degree of dehydration of the nanostructures, as explained in a previous work [20]. Other authors have also observed a change in WO_3 nanostructures morphology with annealing temperature [21–26]. Concerning the influence of annealing atmosphere on the morphology and size of WO_3 nanostructures, it can be observed that samples treated in air and N_2 were similar, regardless of the temperature (**Figures 1a-1c** (air) and **Figures 1g-1i** (Ar)). The samples annealed in an Ar atmosphere at 400º C and 500º C (**Figure 1g** and **Figure 1h**) were also similar to the ones annealed at the same temperature under air and N_2. However, at 600º C, the sample annealed in Ar was different, since nanorods were not observed. Instead, very small and deformed nanoplates or nanoparticles were obtained. This morphology might prevent photogenerated charges from being

efficiently separated, hence reducing photoelectrochemical performance of nanostructures.

Figure 2 shows the Raman spectra of all the WO_3 samples. The shape of all the spectra is similar, regardless of the annealing conditions. Characteristics peaks of crystalline WO_3 are observed in the plots: 125 cm^{-1}, 195 cm^{-1}, 275 cm^{-1}, 715 cm^{-1} and 822 cm^{-1} [27–29]. However, there are some differences. At 400º C, a very low-intensity band can be discerned at around 940-950 cm^{-1}, as well as a shoulder at ~650 cm^{-1}, which has been associated habitually with amorphous hydrated WO_3 ($WO_3 \cdot xH_2O$) [27–30]. These bands disappeared as annealing temperature increased in air and N_2 atmospheres (**Figure 2a** and **Figure 2b**), indicating a higher degree of dehydration and crystallinity of nanostructures treated under those conditions. At 600º C for air and N_2 atmospheres (**Figure 2a** and **Figure 2b**), the peak centered at 330 cm^{-1} became much clearer. This peak has also been related to crystalline WO_3 [27–29], confirming a higher crystallinity of samples annealed at 600º C in air an N_2 atmospheres. On the other hand, spectra of samples treated at 600º C in Ar atmosphere (**Figure 2c**) did not show the same tendency as samples annealing in the other atmospheres. Therefore, it can be said that this sample was less crystalline than the other samples annealed at the same temperature in other gaseous atmospheres.

The photoelectrocatalytic performance of the different nanostructures is shown in **Figure 3**. In this figure, the mean photocurrent density (i_{ph}) obtained under simulated solar light, applying an external potential of $1V_{Ag/AgCl}$ and after 30 min of stabilization, is represented for each temperature and annealing atmosphere. It can be seen that i_{ph}

values increased, in general, with increasing annealing temperature for all the atmospheres, except for the sample annealed in Ar at 600º C. The enhancement of photoelectrocatalytic performance with annealing temperature can be explained by a better crystallinity [25,26,31–33], as observed in Raman spectra, as well as by the nanorod morphology obtained at high temperatures, which has been associated before with a better electronic transport through the WO_3 nanostructure. In fact, the transition from poorly ordered nanosheets at 400º C to defined and ordered nanorods at 600º C can enhance electron and hole transfer within the nanostructure, hence increasing the photoelectrochemical performance of samples annealed at high temperatures [21]. According to **Figure 3**, the best photoelectrochemical performance corresponded to the nanostructure annealed at 600º C in an air atmosphere.

In order to study the mechanism of photocurrent generation in the WO_3 nanostructures, and the influence of annealing conditions on the different electrochemical and photoelectrochemical phenomena taking place in the irradiated semiconducting nanostructures, Photoelectrochemical Impedance Spectroscopy (PEIS) experiments have been carried out. **Figure 4** and **Figure 5** show the Nyquist and Bode-phase plots under illumination for the different WO_3 nanostructures, respectively. At first sight, only one semicircle was perceptible in the Nyquist plots. However, at high frequencies, a very small semicircle was also present (not shown). Besides, two peaks in Bode-phase plot for the sample annealed in air at 400º C could be clearly discerned, and a wide peak was evident in the rest of Bode plots, probably indicating the overlapping of two individual peaks. In Nyquist plots (**Figure 4**), the high-amplitude semicircle obtained at intermediate and low frequencies decreased, in general, with increasing annealing temperatures for all the atmospheres. When working with nanostructured semiconductor

under illumination conditions, this semicircle has usually been associated in the literature with the charge transfer of holes from either the valence band or surface states to the electrolyte [34–38], where they can oxidize the media to form species such as gaseous oxygen, hydroxyl radicals, oxidized organic matter, etc. Therefore, the low frequency semicircle related to charge transfer of holes dominated the impedance response of all the samples. Hence, the decrease of impedance values with increasing annealing temperatures indicates a better photoelectrochemical response of the nanostructures treated at 600º C in air and N_2 atmospheres. However, in Ar atmosphere, is spite of the semicircle being similar in amplitude for the samples annealed at 500º C and 600º C, the photoelectrochemical response was lower at 600º C, due to morphology differences (see **Figure 1i**). The previous results are consistent with the photocurrent density responses observed above (**Figure 3**). To quantitatively analyze impedance results, an electric equivalent circuit has been used (**Figure 6**). In this circuit, R_S is the electrolyte resistance, the first R_1-CPE_1 time constant has been related to electron-hole trapping in surface states or in the bulk semiconductor, while the second R_2-CPE_2 time constant has been associated with hole transfer from WO_3 to the electrolyte [35–38]. Constant Phase Elements (*CPE*) have been used in this equivalent circuit to take into account the non-ideality of electrochemical capacitances.

Values of the resistances that make up the equivalent circuit are shown in **Table 1** for all the samples. It can be observed that R_1 was always much lower than R_2, as expected. In general, R_2 decreased with increasing annealing temperature, indicating enhanced charge transfer of holes from the nanostructure to the electrolyte. A similar trend was observed by Zhu et al. [25]. In the case of the sample annealed at 600º C in an Ar atmosphere, it can be seen that the value of R_2 was higher than at 500º C in the same

annealing atmosphere. This fact may be related to the morphology of nanostructures explained above, since at 600º C in Ar, deformed nanoplates were obtained (**Figure 1i**), which increased the charge transfer resistance of holes from the nanostructure to the electrolyte.

Impedance results can also be used to determine the density of dopants in a semiconductor, by means of the Mott-Schottky equation for an *n*-type semiconductor (such as WO_3):

$$\frac{1}{C^2} = \frac{1}{C_H^2} + \frac{2}{\varepsilon_r \varepsilon_0 e N_D}\left(E - E_{FB} - \frac{kT}{e}\right) \quad \textbf{(1)}$$

where C is the measured total interfacial capacitance, C_H is the capacitance of the Helmholtz layer, ε_r is the dielectric constant of the semiconductor (50 for WO_3 nanostructures [23,39–41]), ε_0 is the permittivity of free space ($8.85 \cdot 10^{-14}$ F/cm), e is the elementary charge ($1.60 \cdot 10^{-19}$ C), N_D is the density of donors in the semiconductor, E is the applied potential, E_{EF} is the flat-band potential, k is the Boltzmann constant ($1.38 \cdot 10^{-23}$ J/K) and T is the absolute temperature.

According to equation (1), a plot of $1/C^2$ vs E should have a linear region with positive slope (for an *n*-type semiconductor), from which the value of N_D can be obtained. Mott-Schottky plots are shown in **Figure 7**. In all cases, a linear region with positive slope can be observed (marked in the plots). This region is related to the presence of donor species within the crystalline structure of WO_3, such as W^{6+} interstitials or oxygen

vacancies. For samples annealed in N_2 and Ar atmospheres, besides, another linear region with a much lower slope can be clearly observed at high potentials, especially for samples annealed at 400º C. The presence of this linear region at high potentials in the Mott-Schottly plots can be attributed to near-surface deep-level electronic states which are potential dependant [42,43] and that can therefore be charged or discharged, or to an unknown geometric factor [43]. The nature of these electronic states is not identified, although their relation with non-oxidizing atmospheres during annealing is evident.

All samples provided lower $1/C^2$ values (higher capacitance values) and lower slopes when increasing annealing temperature, regardless of the used atmosphere. Results of density of donors are presented in **Table 2**. It can be seen that N_D for samples annealed at 400º C and 500º C are similar, although slightly higher at 500º C. However, at 600º C, N_D extensively increased for all samples, especially for the one annealed in the N_2 atmosphere. In general, there is a correlation between high photocurrent densities, low charge transfer resistances (R_2) and high donor densities (N_D). It is reasonable, since a high density of donor species would result in higher mobility of electron and holes within the WO_3 nanostructures, hence reducing charge transfer resistances and enhancing the photoelectrochemical performance of photoanodes.

The sample annealed at 600º C and in an air atmosphere has provided the highest photocurrent density values, showing an excellent photoelectrochemical behavior. This photoanode is, therefore, suitable to be used as high efficient photoelectrocatalysts in many environmental and energy applications. Consequently, besides presenting an extensive characterization procedure to investigate the properties of

photoelectrocatalysts, the present work can contribute in an important way to the progress in photoelectrochemical technology applied to the environmental (degradation of recalcitrant organic pollutants, such as pesticides) and energy (generation of H_2 through photoelectrochemical water splitting) fields.

CONCLUSIONS

- WO_3 nanosheets were obtained annealing at 400º C, while nanorods were obtained at higher annealing temperatures (600º C). In the Ar atmosphere at 600º C, nanostructures were deformed.
- As temperature increased from 400º C to 600º C, samples became completely crystalline and dehydrated.
- The best photoelectrochemical performance was obtained for the sample treated at 600º C in air. For samples annealed in Ar, photocurrent densities decreased at 600º C due to the poorly defined nanostructures.
- Hole transfer resistance decreased in general with increasing annealing temperatures, indicating enhanced charge transfer of holes and, consequently, improved photoelectrocatalytic properties.
- The density of dopant species (donor) increased with increasing annealing temperature. Therefore, there is a direct correlation between high photocurrent densities, low hole transfer resistances and high donor densities.

Aknowledgements

Authors thank for the financial support to the Ministerio de Economía y Competitividad (Project Codes: CTQ2016-79203-R and CTQ2017-90659-REDT (MEIS/AEI)), for its help in the Laser Raman Microscope acquisition (UPOV08-3E-012) and for the co-finance by the European Social Fund. Ramón M. Fernández Domene also thanks the UPV for the concession of a post-doctoral grant (PAID-10-17) and Gemma Roselló Márquez also thanks the Generalitat Valenciana for the concession of a pre-doctoral grant (ACIF/2018/159).

REFERENCES

[1] Y.M. Hunge, V.S. Mohite, S.S. Kumbhar, K.Y. Rajpure, A. V. Moholkar, C.H. Bhosale, Photoelectrocatalytic degradation of methyl red using sprayed WO_3 thin films under visible light irradiation, J. Mater. Sci. Mater. Electron. 26 (2015) 8404–8412. doi:10.1007/s10854-015-3508-z.

[2] Y.M. Hunge, A.A. Yadav, M.A. Mahadik, V.L. Mathe, C.H. Bhosale, A highly efficient visible-light responsive sprayed WO_3/FTO photoanode for photoelectrocatalytic degradation of brilliant blue, J. Taiwan Inst. Chem. Eng. 85 (2018) 273–281. doi:10.1016/j.jtice.2018.01.048.

[3] M. Rakibuddin, H. Kim, Synthesis and characterization of facile industrially scalable and cost effective WO_3 micro–nanostructures for electrochromic devices and photocatalyst, Ceram. Int. 44 (2018) 16615–16623. doi:10.1016/j.ceramint.2018.06.088.

[4] A.F. Palmstrom, P.K. Santra, S.F. Bent, Atomic layer deposition in nanostructured photovoltaics: tuning optical, electronic and surface properties, Nanoscale. 7 (2015) 12266–12283. doi:10.1039/c5nr02080h.

[5] C. Di Valentin, G. Pacchioni, Spectroscopic properties of doped and defective semiconducting oxides from hybrid density functional calculations, Acc. Chem. Res. 47 (2014) 3233–3241. doi:10.1021/ar4002944.

[6] J. Zhang, X. Chang, C. Li, A. Li, S. Liu, T. Wang, J. Gong, WO_3 photoanodes with controllable bulk and surface oxygen vacancies for photoelectrochemical water oxidation, J. Mater. Chem. A. 6 (2018) 3350–3354. doi:10.1039/c7ta10056f.

[7] Z.F. Huang, J. Song, L. Pan, X. Zhang, L. Wang, J.J. Zou, Tungsten oxides for photocatalysis, electrochemistry, and phototherapy, Adv. Mater. 27 (2015) 5309–5327. doi:10.1002/adma.201501217.

[8] Y.M. Hunge, M.A. Mahadik, S.S. Kumbhar, V.S. Mohite, K.Y. Rajpure, N.G. Deshpande, A. V. Moholkar, C.H. Bhosale, Visible light catalysis of methyl orange using nanostructured WO_3 thin films, Ceram. Int. 42 (2016) 789–798. doi:10.1016/j.ceramint.2015.08.178.

[9] J. Zhu, W. Li, J. Li, Y. Li, H. Hu, Y. Yang, Photoelectrochemical activity of $NiWO_4/WO_3$ heterojunction photoanode under visible light irradiation, Electrochim. Acta. 112 (2013) 191–198. doi:10.1016/j.electacta.2013.08.146.

[10] S.S. Kalanur, L.T. Duy, H. Seo, Recent Progress in Photoelectrochemical Water Splitting Activity of WO_3 Photoanodes, Springer US, 2018. doi:10.1007/s11244-

018-0950-1.

[11] D.W. Bullet, Bulk and surface electron states in WO_3 and tungsten bronzes, J. Phys. C: Solid State Phys., 16 (1983) 2197-2207.

[12] S.S. Kalanur, Y.J. Hwang, S.Y. Chae, O.S. Joo, Facile growth of aligned WO_3 nanorods on FTO substrate for enhanced photoanodic water oxidation activity, J. Mater. Chem. A 1 (2013) 3479–3488. doi:10.1039/c3ta01175e.

[13] D.B. Migas, V. L. Shaposhnikov, V. N. Rodin, V. E. Borisenko, Tungsten oxides. I. Effects of oxygen vacancies and doping on electronic and optical properties of different phases of WO_3, J. Appl. Phys. 108 (2010) 093713. doi:10.1063/1.3505688.

[14] Á. Valdés, G.-J. Kroes, First principles study of the photo-oxidation of water on tungsten trioxide (WO_3), J. Appl. Phys. 130 (2009) 114701. doi:10.1063/1.3088845.

[15] Y. Guo, X. Quan, N. Lu, H. Zhao, S. Chen, High Photocatalytic Capability of Self-Assembled Nanoporous WO_3 with Preferential Orientation of (002) Planes, Environ. Sci. Technol. 41 (2007) 4422-4427.

[16] Y. Liu, Y. Li, W. Li, S. Han, C. Liu, Applied Surface Science Photoelectrochemical properties and photocatalytic activity of nitrogen-doped nanoporous WO_3 photoelectrodes under visible light, 258 (2012) 5038–5045. doi:10.1016/j.apsusc.2012.01.080.

[17] C. Ng, Y.H. Ng, A. Iwase, R. Amal, Influence of Annealing Temperature of WO_3 in Photoelectrochemical Conversion and Energy Storage for Water Splitting, ACS Appl. Mater. Interfaces 5 (2013) 5269-5275. doi: 10.1021/am401112q

[18] S.J. Hong, H. Jun, P.H. Borse, J.S. Lee, Size effects of WO_3 nanocrystals for photooxidation of water in particulate suspension and photoelectrochemical film systems, Int. J. Hydrogen Energy. 34 (2009) 3234–3242. doi:10.1016/j.ijhydene.2009.02.006.

[19] T. Zhu, M. Nan, Y. Wen, E. Chan, Colloids and Surfaces A : Physicochemical and Engineering Aspects Electrochemically synthesized tungsten trioxide nanostructures for photoelectrochemical water splitting : Influence of heat treatment on physicochemical properties, photocurrent densities, Colloids Surfaces A Physicochem. Eng. Asp. 484 (2015) 297–303. doi:10.1016/j.colsurfa.2015.08.016.

[20] R.M. Fernández-Domene, G. Roselló-Márquez, R. Sánchez-Tovar, B. Lucas-Granados, J. García-Antón, Photoelectrochemical removal of chlorfenvinphos by using WO_3 nanorods: Influence of annealing temperature and operation pH, Sep. Purif. Technol. 212 (2019) 458–464. doi:10.1016/j.seppur.2018.11.049.

[21] X. Fan, B. Gao, T. Wang, X. Huang, H. Gong, H. Xue, H. Guo, L. Song, W. Xia, J. He, Layered double hydroxide modified WO_3 nanorod arrays for enhanced photoelectrochemical water splitting, Appl. Catal. A Gen. 528 (2016) 52–58. doi:10.1016/j.apcata.2016.09.014.

[22] S.J. Hong, H. Jun, P.H. Borse, J.S. Lee, Size effects of WO_3 nanocrystals for photooxidation of water in particulate suspension and photoelectrochemical film systems, Int. J. Hydrogen Energy. 34 (2009) 3234–3242. doi:10.1016/j.ijhydene.2009.02.006.

[23] Y. Liu, Y. Li, W. Li, S. Han, C. Liu, Photoelectrochemical properties and photocatalytic activity of nitrogen-doped nanoporous WO_3 photoelectrodes under visible light, Appl. Surf. Sci. 258 (2012) 5038–5045. doi:10.1016/j.apsusc.2012.01.080.

[24] C. Ng, Y.H. Ng, A. Iwase, R. Amal, Influence of annealing temperature of WO_3 in photoelectrochemical conversion and energy storage for water splitting, ACS Appl. Mater. Interfaces. 5 (2013) 5269–5275. doi:10.1021/am401112q.

[25] T. Zhu, M.N. Chong, Y.W. Phuan, E.S. Chan, Electrochemically synthesized tungsten trioxide nanostructures for photoelectrochemical water splitting: Influence of heat treatment on physicochemical properties, photocurrent densities and electron shuttling, Colloids Surfaces A Physicochem. Eng. Asp. 484 (2015) 297–303. doi:10.1016/j.colsurfa.2015.08.016.

[26] Y. Chai, C.W. Tam, K.P. Beh, F.K. Yam, Z. Hassan, Effects of thermal treatment on the anodic growth of tungsten oxide films, Thin Solid Films. 588 (2015) 44–49. doi:10.1016/j.tsf.2015.04.033.

[27] M.F. Daniel, B. Desbat, J.C. Lassegues, B. Gerand, M. Figlarz, Infrared and Raman study of WO_3 tungsten trioxides and WO_3, xH_2O tungsten trioxide tydrates, J. Solid State Chem. 67 (1987) 235–247. doi:10.1016/0022-4596(87)90359-8.

[28] C. Bittencourt, R. Landers, E. Llobet, X. Correig, J. Calderer, The role of oxygen partial pressure and annealing temperature on the formation of W=O bonds in thin WO_3 films, Semicond. Sci. Technol. 17 (2002) 522–525. doi:10.1088/0268-

1242/17/6/304.

[29] C.K. Wang, C.K. Lin, C.L. Wu, S.C. Wang, J.L. Huang, Synthesis and characterization of electrochromic plate-like tungsten oxide films by acidic treatment of electrochemical anodized tungsten, Electrochim. Acta. 112 (2013) 24–31. doi:10.1016/j.electacta.2013.07.204.

[30] S.H. Lee, H.M. Cheong, C.E. Tracy, A. Mascarenhas, D.K. Benson, S.K. Deb, Raman spectroscopic studies of electrochromic a-WO_3, Electrochim. Acta. 44 (1999) 3111–3115. doi:10.1016/S0013-4686(99)00027-4.

[31] K.S. Ahn, S.H. Lee, A.C. Dillon, C.E. Tracy, R. Pitts, The effect of thermal annealing on photoelectrochemical responses of WO_3 thin films, J. Appl. Phys. 101 (2007) 1–5. doi:10.1063/1.2729472.

[32] Y.W. Phuan, M.N. Chong, T. Zhu, S.T. Yong, E.S. Chan, Effects of annealing temperature on the physicochemical, optical and photoelectrochemical properties of nanostructured hematite thin films prepared via electrodeposition method, Mater. Res. Bull. 69 (2015) 71–77. doi:10.1016/j.materresbull.2014.12.059.

[33] Q. Zeng, J. Li, J. Bai, X. Li, L. Xia, B. Zhou, Preparation of vertically aligned WO_3 nanoplate array films based on peroxotungstate reduction reaction and their excellent photoelectrocatalytic performance, Appl. Catal. B Environ. 202 (2017) 388–396. doi:10.1016/j.apcatb.2016.09.045.

[34] W.H. Leng, Z. Zhang, J.Q. Zhang, C.N. Cao, Investigation of the kinetics of a TiO_2 photoelectrocatalytic reaction involving charge transfer and recombination through surface states by electrochemical impedance spectroscopy, J. Phys. Chem. B. 109 (2005) 15008–15023. doi:10.1021/jp051821z.

[35] B. Klahr, S. Gimenez, F. Fabregat-Santiago, T. Hamann, J. Bisquert, Water oxidation at hematite photoelectrodes: The role of surface states, J. Am. Chem. Soc. 134 (2012) 4294–4302. doi:10.1021/ja210755h.

[36] L. Bertoluzzi, J. Bisquert, Equivalent circuit of electrons and holes in thin semiconductor films for photoelectrochemical water splitting applications, J. Phys. Chem. Lett. 3 (2012) 2517–2522. doi:10.1021/jz3010909.

[37] L. Bertoluzzi, P. Lopez-Varo, J.A. Jiménez Tejada, J. Bisquert, Charge transfer processes at the semiconductor/electrolyte interface for solar fuel production: Insight from impedance spectroscopy, J. Mater. Chem. A. 4 (2016) 2873–2879. doi:10.1039/c5ta03210e.

[38] V. Cristino, S. Marinello, A. Molinari, S. Caramori, S. Carli, R. Boaretto, R. Argazzi, L. Meda, C.A. Bignozzi, Some aspects of the charge transfer dynamics in nanostructured WO_3 films, J. Mater. Chem. A. 4 (2016) 2995–3006. doi:10.1039/c5ta06887h.

[39] M. Yagi, S. Maruyama, K. Sone, K. Nagai, T. Norimatsu, Preparation and photoelectrocatalytic activity of a nano-structured WO_3 platelet film, J. Solid State Chem. 181 (2008) 175–182. doi:10.1016/j.jssc.2007.11.018.

[40] W. Li, J. Li, X. Wang, J. Ma, Q. Chen, Photoelectrochemical and physical properties of WO_3 films obtained by the polymeric precursor method, Int. J. Hydrogen Energy. 35 (2010) 13137–13145. doi:10.1016/j.ijhydene.2010.09.011.

[41] F. Amano, M. Tian, B. Ohtani, A. Chen, Photoelectrochemical properties of tungsten trioxide thin film electrodes prepared from facet-controlled rectangular platelets, J. Solid State Electrochem. 16 (2012) 1965–1973. doi:10.1007/s10008-011-1586-2.

[42] D.. Bonham, M.E. Orazem, A Mathematical Model for the Influence of Deep—Level Electronic States on Photoelectrochemical Impedance Spectroscopy. I. Theoretical Development, J. Electrochem. Soc. 139 (1992) 118–126. doi:10.1149/1.2069155.

[43] K. Siuzdak, M. Szkoda, M. Sawczak, A. Lisowska-Oleksiak, J. Karczewski, J. Ryl, Enhanced photoelectrochemical and photocatalytic performance of iodine-doped titania nanotube arrays, RSC Adv. 5 (2015) 50379–50391. doi:10.1039/c5ra08407e.

Tables and Figures captions

Table 1. Resistance values of the the WO_3 nanostructures annealed at different temperatures and in different atmospheres.

Table 2. Density of donors, N_D, of the the WO_3 nanostructures annealed at different temperatures and in different atmospheres.

Figure 1. FESEM images of the WO_3 nanostructures annealed in an air atmosphere at a) 400º C, b) 500º C and c) 600º C; in a N_2 atmosphere at d) 400º C, e) 500º C and f) 600º C; in an Ar atmosphere at g) 400º C; h) 500º C and i) 600º C.

Figure 2. Raman spectra of WO_3 nanostructures annealed at different temperatures in a) air; b) N_2 and c) Ar.

Figure 3. Mean values of photocurrent density for the WO_3 nanostructures annealed at different temperatures and in different atmospheres, obtained under simulated solar light applying an external potential of $1V_{Ag/AgCl}$ and after 30 min of stabilization

Figure 4. Nyquist plots under simulated solar light AM1.5 for the WO_3 nanostructures annealed at different temperatures in a) air; b) N_2 and c) Ar.

Figure 5. Bode-phase plots under simulated solar light AM1.5 for the WO_3 nanostructures annealed at different temperatures in a) air; b) N_2 and c) Ar.

Figure 6. Electric equivalent circuit used to analyze EIS data.

Figure 7. Mott-Schottky plots under simulated solar light AM1.5 for the WO_3 nanostructures annealed at different temperatures in a) air; b) N_2 and c) Ar.

Figure 1

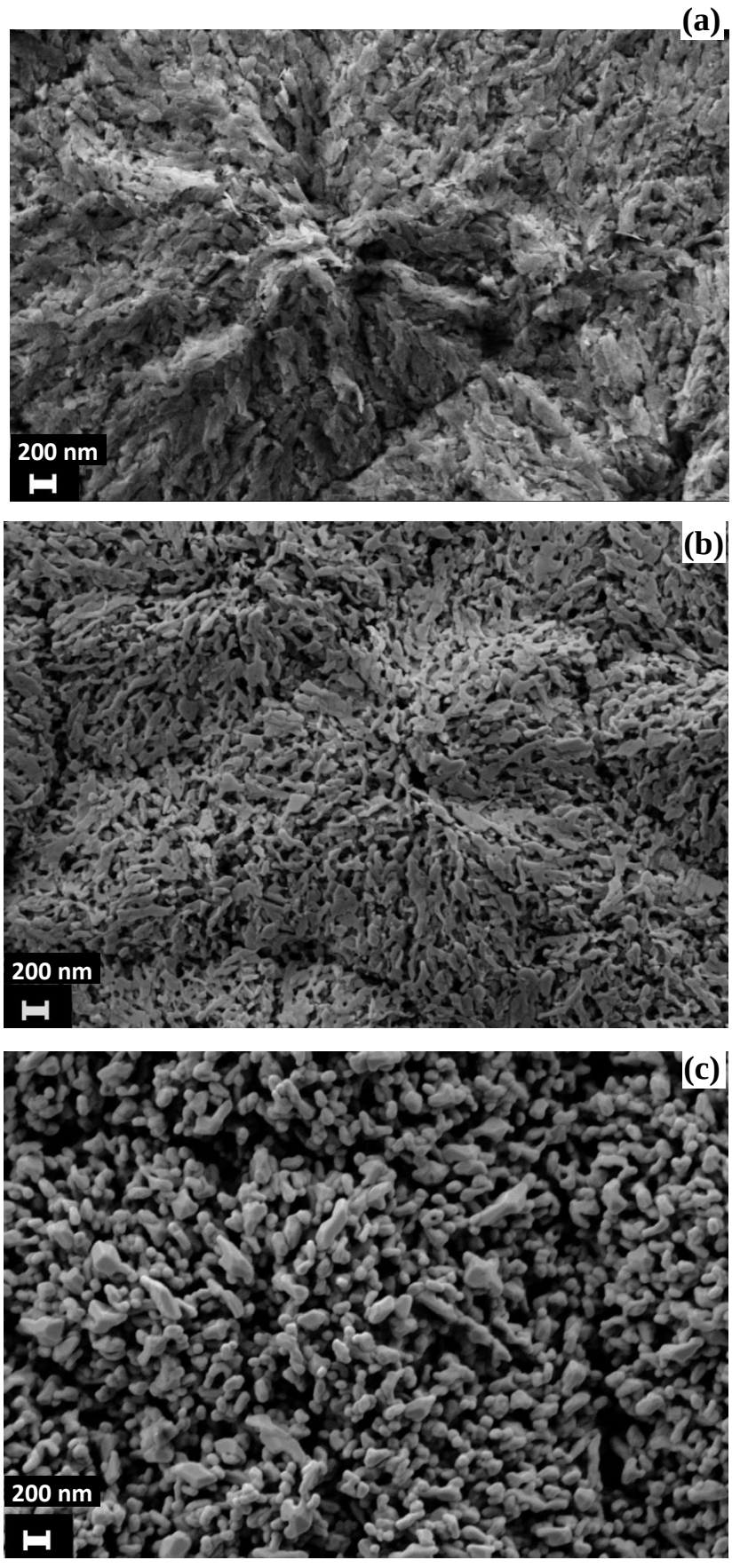

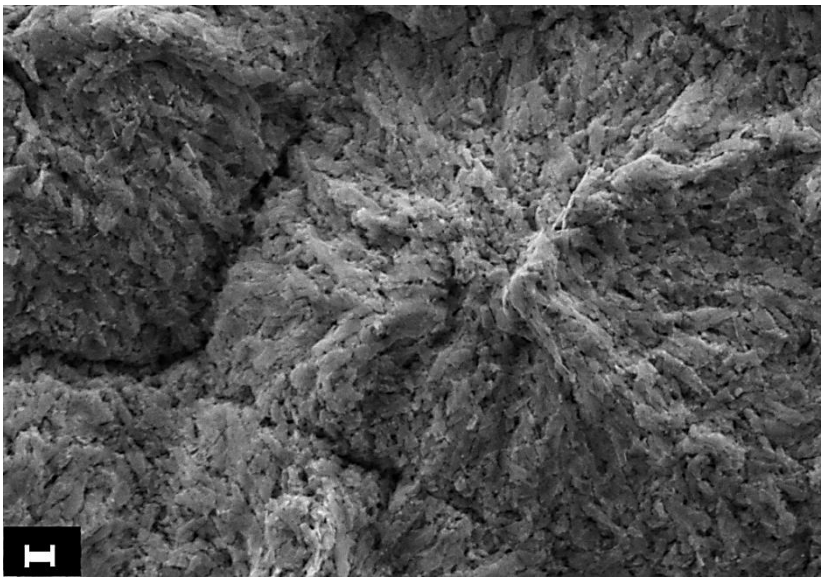

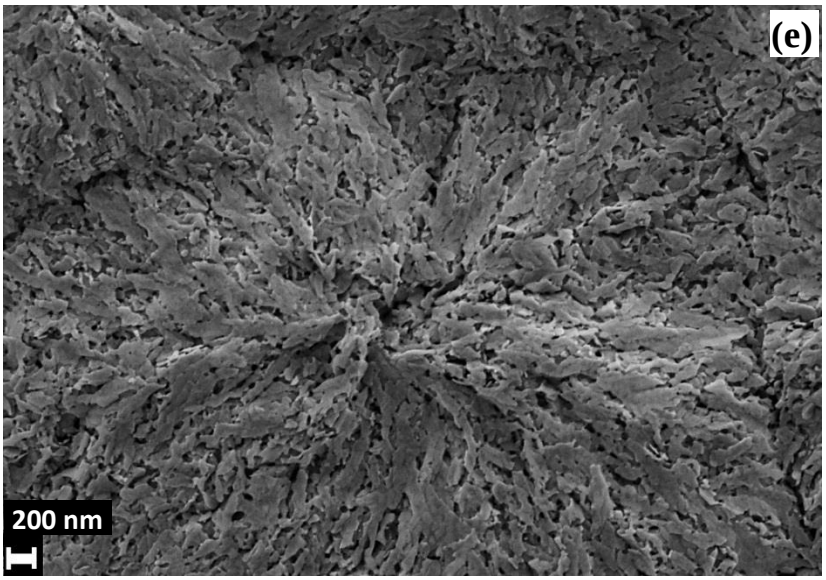

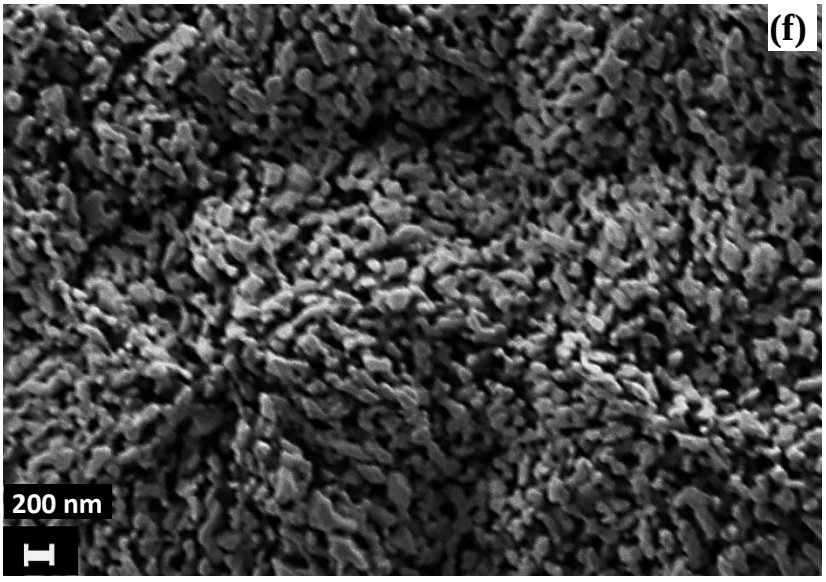

(g)

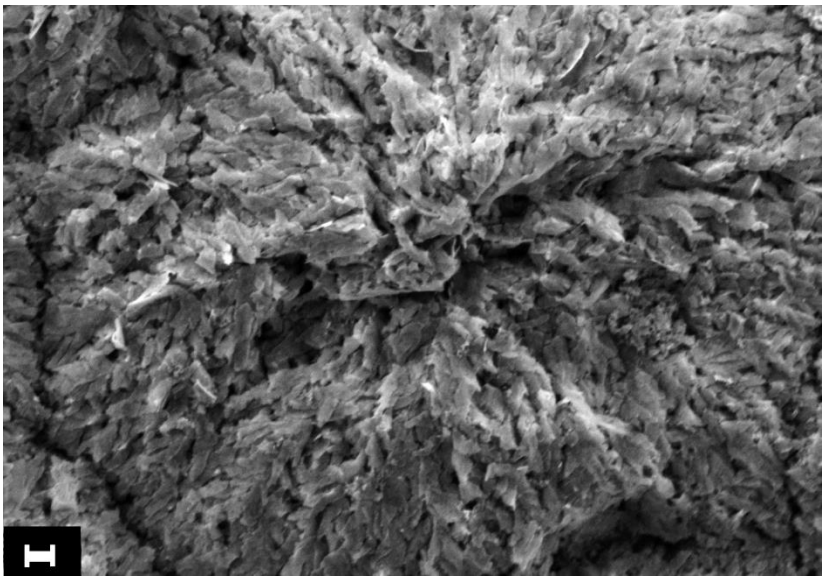

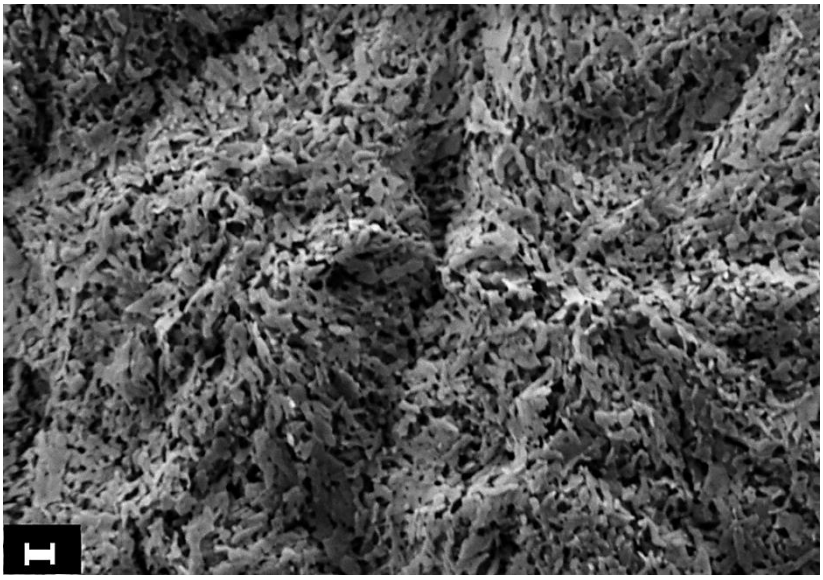

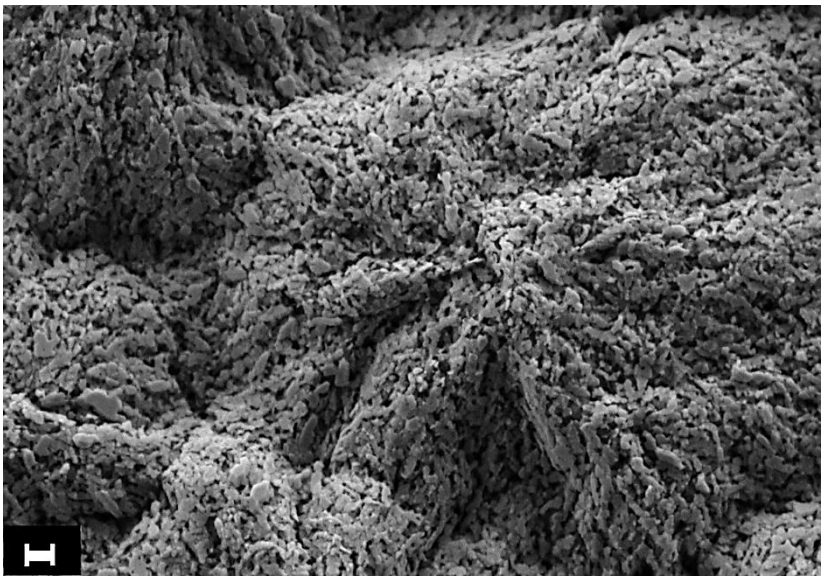

Figure 2

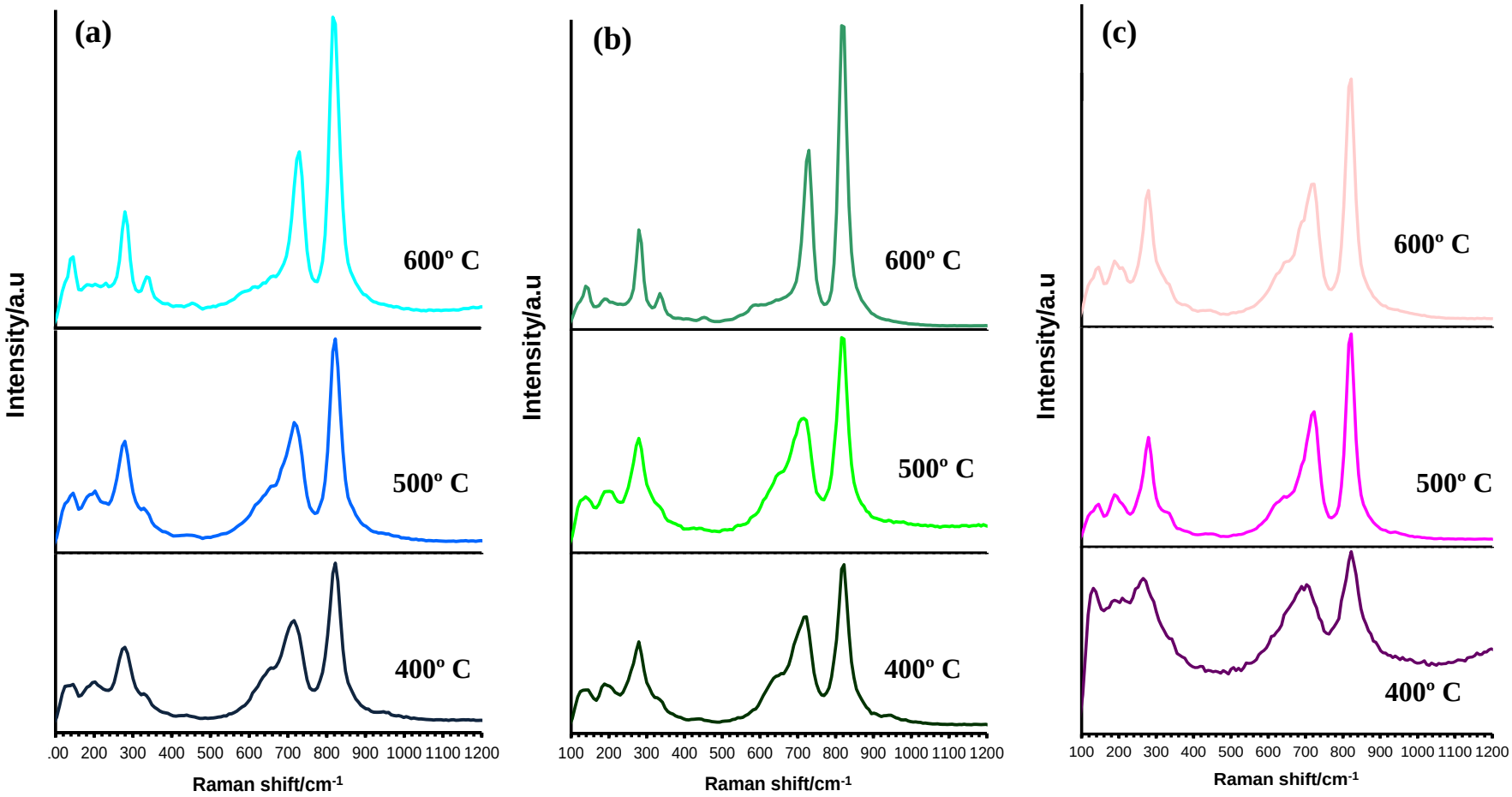
(a)
600º C
500º C
400º C
Intensity/a.u
.00 200 300 400 500 600 700 800 900 1000 1100 1200
Raman shift/cm-1
(b)
600º C
500º C
400º C
Intensity/a.u
100 200 300 400 500 600 700 800 900 1000 1100 1200
Raman shift/cm-1
(c)
600º C
500º C
400º C
Intensity/a.u
100 200 300 400 500 600 700 800 900 1000 1100 1200
Raman shift/cm-1

Figure 3

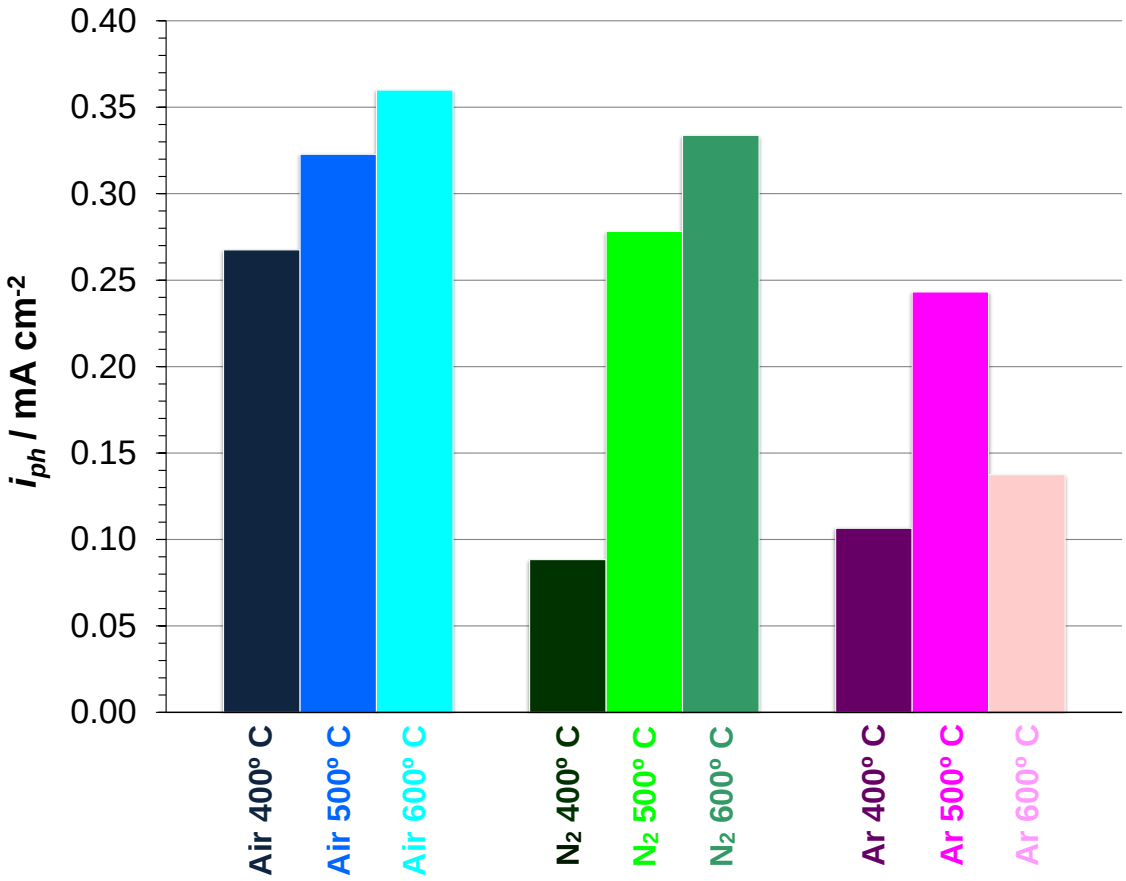
0.40
0.35
0.30
0.25
0.20
0.15
0.10
0.05
0.00
i_{ph} / mA cm^{-2}
Air 400° C
Air 500° C
Air 600° C
N_2 400° C
N_2 500° C
N_2 600° C
Ar 400° C
Ar 500° C
Ar 600° C

Figure 4

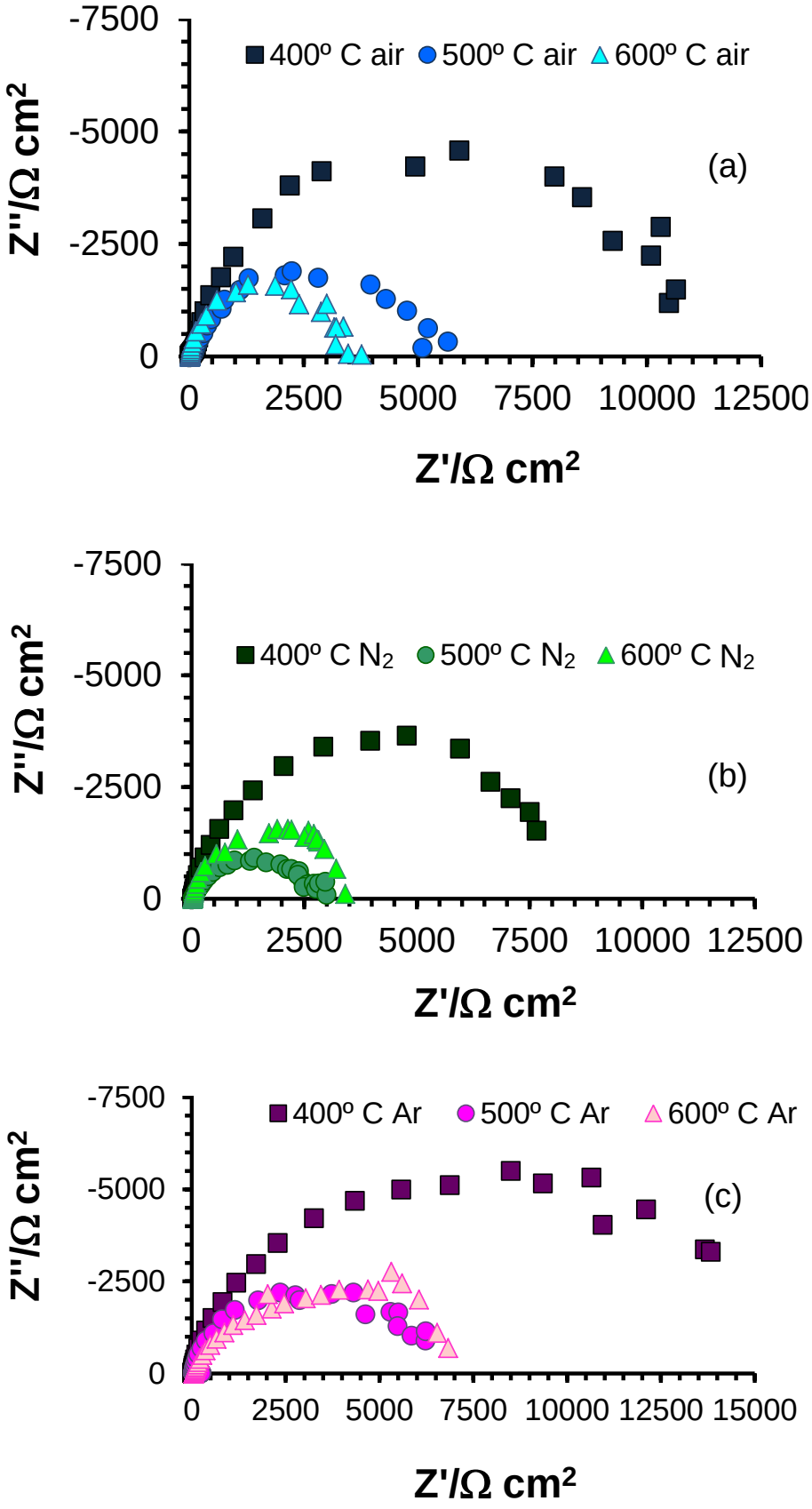
-7500
-5000
-2500
0
Z''/Ω cm²
400º C air
500º C air
600º C air
(a)
0
2500
5000
7500
10000
12500
Z'/Ω cm²
-7500
-5000
-2500
0
Z''/Ω cm²
400º C N2
500º C N2
600º C N2
(b)
0
2500
5000
7500
10000
12500
Z'/Ω cm²
-7500
-5000
-2500
0
Z''/Ω cm²
400º C Ar
500º C Ar
600º C Ar
(c)
0
2500
5000
7500
10000
12500
15000
Z'/Ω cm²

Figure 5

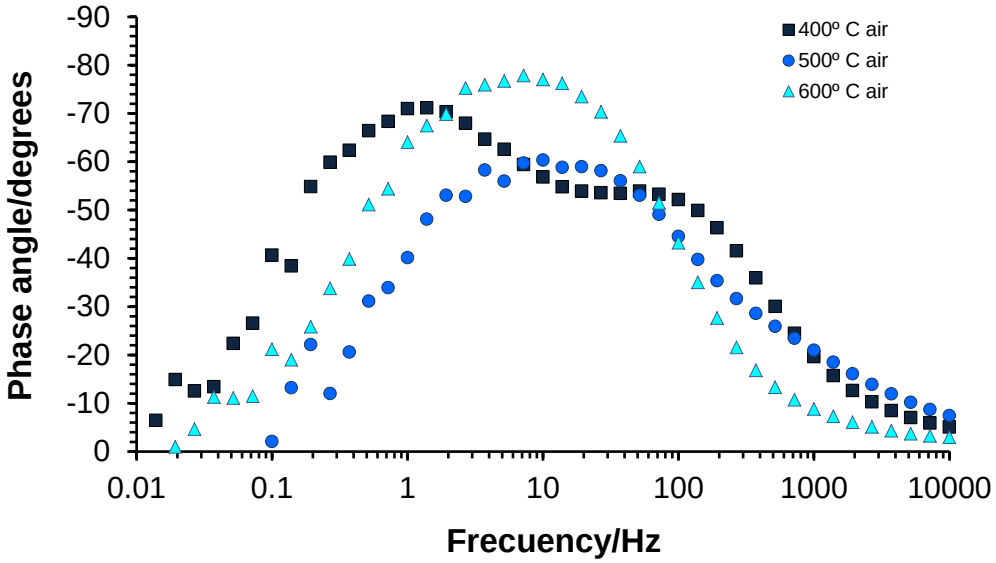
Phase angle/degrees
-90
-80
-70
-60
-50
-40
-30
-20
-10
0
0.01
0.1
1
10
100
1000
10000
Frecuency/Hz
400º C air
500º C air
600º C air

(a)

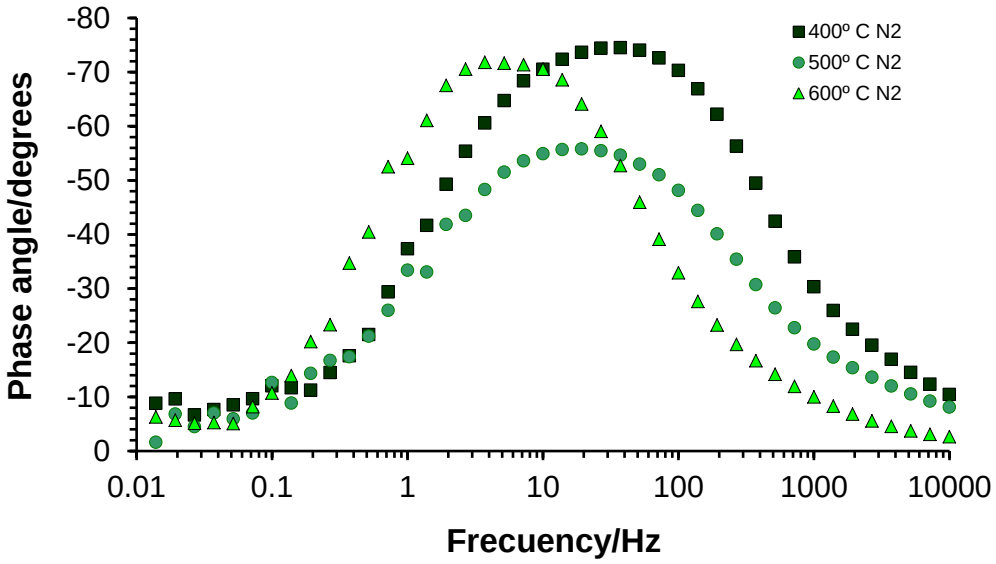
Phase angle/degrees
-80
-70
-60
-50
-40
-30
-20
-10
0
0.01
0.1
1
10
100
1000
10000
Frecuency/Hz
400º C N2
500º C N2
600º C N2
N2
N2
N2

(b)

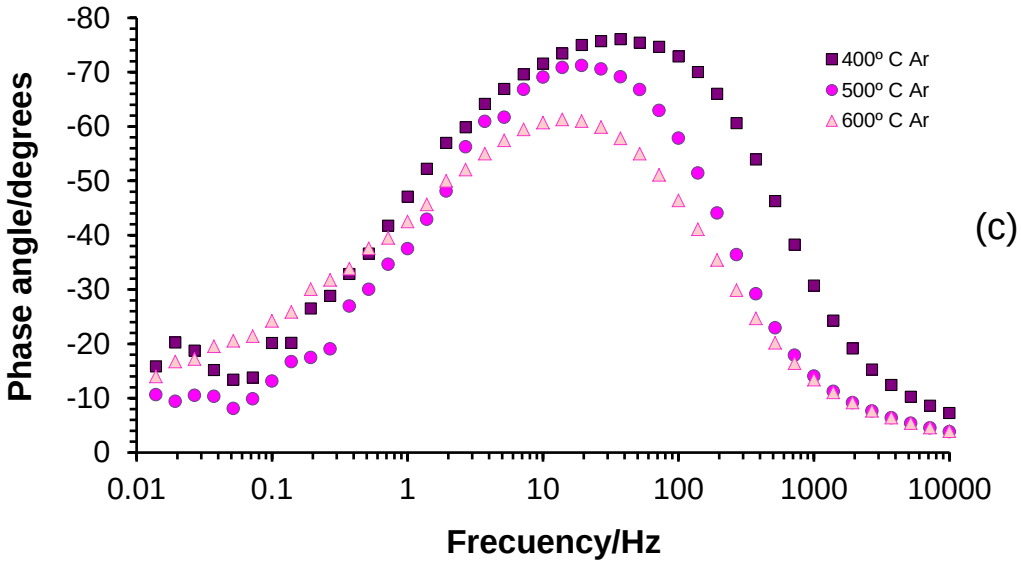
Phase angle/degrees
-80
-70
-60
-50
-40
-30
-20
-10
0
0.01
0.1
1
10
100
1000
10000
Frecuency/Hz
400º C Ar
500º C Ar
600º C Ar
(c)

Figure 6

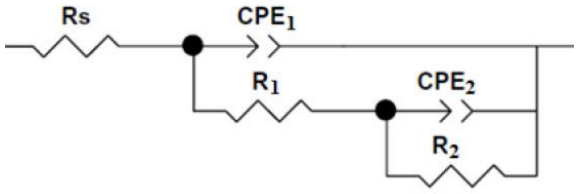
Rs
CPE1
R1
CPE2
R2

Figure 7

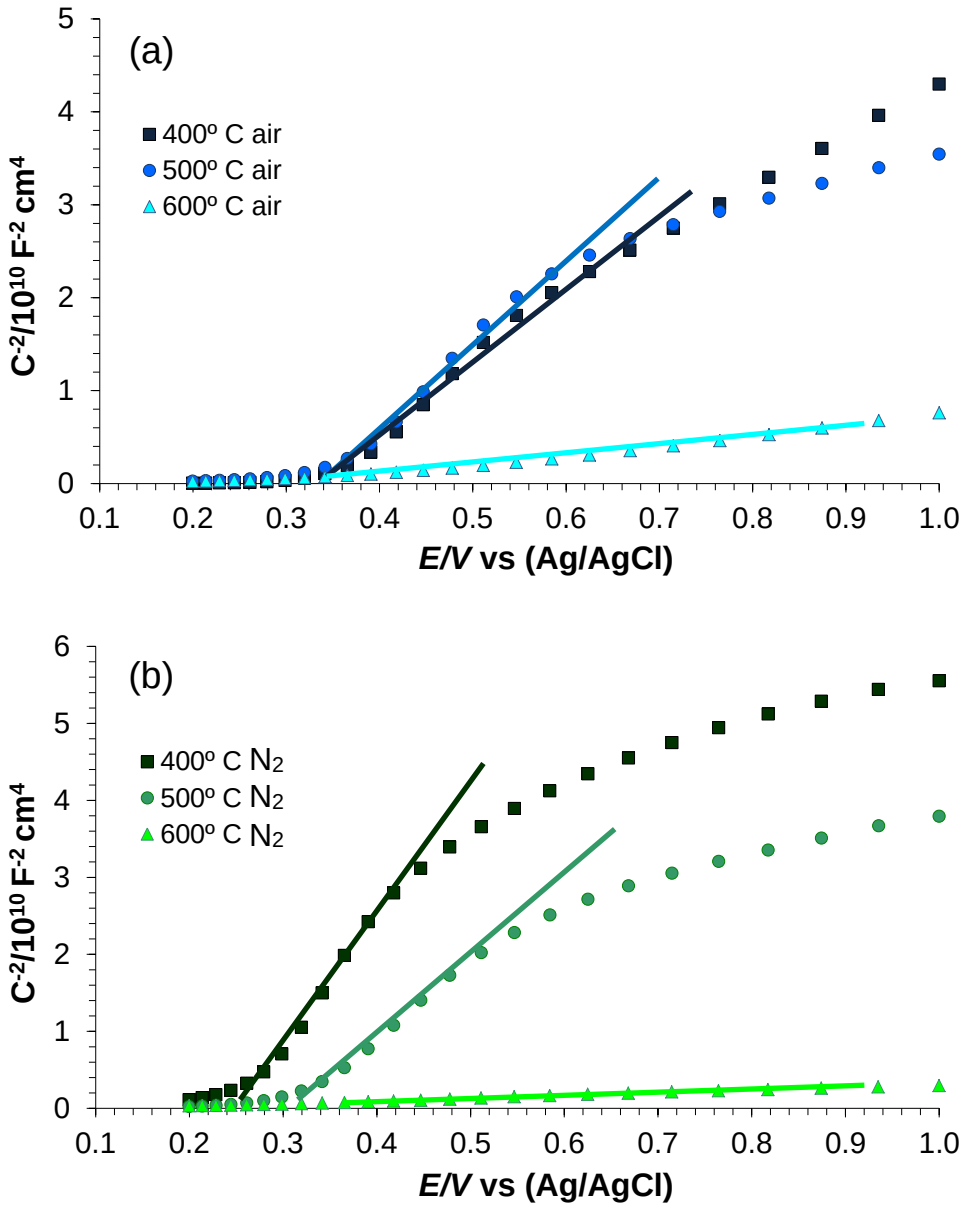
(a)
400º C air
500º C air
600º C air
C-2/1010 F-2 cm4
E/V vs (Ag/AgCl)
(b)
400º C N2
500º C N2
600º C N2
C-2/1010 F-2 cm4
E/V vs (Ag/AgCl)

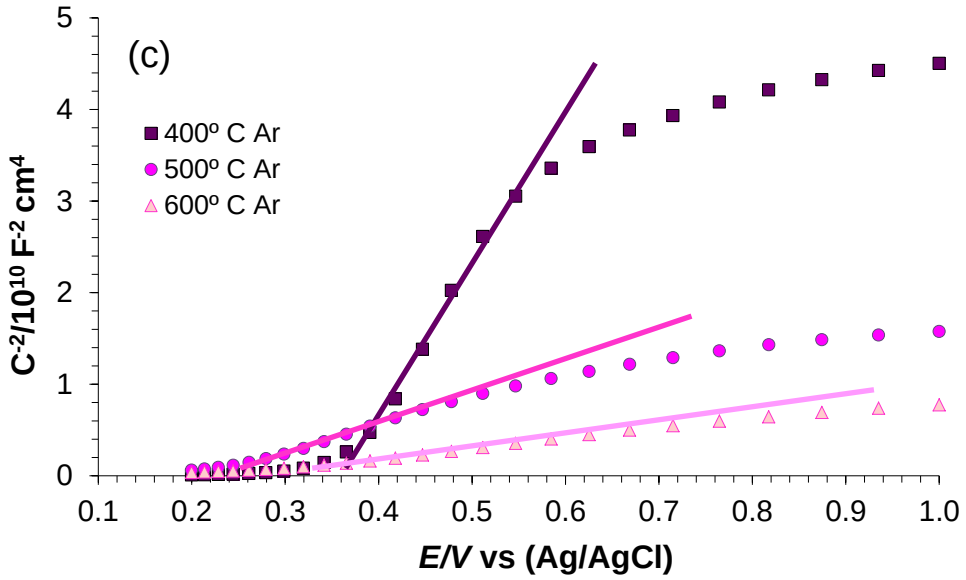

Table 1

Atmosphere	*T/ºC*	$R_S/\Omega\ cm^2$	$R_1/\Omega\ cm^2$	$R_2/k\Omega\ cm^2$
Air	400	29 ± 3	159 ± 11	11.8 ± 1.6
	500	44 ± 9	107 ± 26	7.6 ± 1.3
	600	28 ± 6	26 ± 7	3.0 ± 0.9
N_2	400	27 ± 6	5 ± 1	10.1 ± 4.0
	500	32 ± 2	31 ± 5	2.7 ± 0.3
	600	27 ± 3	22 ± 9	2.9 ± 0.4
Ar	400	37 ± 8	16 ± 2	14.9 ± 0.8
	500	27 ± 1	32 ± 9	7.4 ± 0.1
	600	22 ± 4	21 ±3	9.6 ± 3.7

Table 2

Atmosphere	*T/ºC*	N_D (× 10^{19} cm^{-3})
Air	400	2.6 ± 0.3
	500	2.9 ± 0.5
	600	20.4 ± 8.6
N_2	400	4.7 ± 2.7
	500	5.2 ± 1.5
	600	45.8 ± 27.7
Ar	400	3.3 ± 1.6
	500	4.5 ± 3.6
	600	16.1 ± 7.0